Tensile testing of materials at high temperatures above 1700 °C with *in situ* synchrotron X-ray micro-tomography

Abdel Haboub,[1] Hrishikesh A. Bale,[2] James R. Nasiatka,[1] Brian N. Cox,[3] David B. Marshall,[3] Robert O. Ritchie,[1,2,a)] and Alastair A. MacDowell[1]
[1]*Lawrence Berkeley National Laboratory, Berkeley, California 94720, USA*
[2]*Department of Materials Science and Engineering, University of California, Berkeley, California 94720, USA*
[3]*Teledyne Scientific Company, Thousand Oaks, California 91360, USA*

(Received 23 June 2014; accepted 25 July 2014; published online 14 August 2014)

A compact ultrahigh temperature tensile testing instrument has been designed and fabricated for *in situ* x-ray micro-tomography using synchrotron radiation at the Advanced Light Source, Lawrence Berkeley National Laboratory. It allows for real time x-ray micro-tomographic imaging of test materials under mechanical load at temperatures up to 2300 °C in controlled environments (vacuum or controlled gas flow). Sample heating is by six infrared halogen lamps with ellipsoidal reflectors arranged in a confocal configuration, which generates an approximately spherical zone of high heat flux approximately 5 mm in diameter. Samples are held between grips connected to a motorized stage that loads the samples in tension or compression with forces up to 2.2 kN. The heating chamber and loading system are water-cooled for thermal stability. The entire instrument is mounted on a rotation stage that allows stepwise recording of radiographs over an angular range of 180°. A thin circumferential (360°) aluminum window in the wall of the heating chamber allows the x-rays to pass through the chamber and the sample over the full angular range. The performance of the instrument has been demonstrated by characterizing the evolution of 3D damage mechanisms in ceramic composite materials under tensile loading at 1750 °C. [http://dx.doi.org/10.1063/1.4892437]

I. INTRODUCTION

Next-generation aerospace and gas-turbine engines are being developed with a primary focus of increasing overall engine efficiency, which will be achieved principally through structural weight reduction by using materials with high specific strength-to-weight ratio and by raising the operating temperatures of the engine.[1] Currently, the range of materials that meet both of these objectives is limited, with ceramic-matrix composites (CMCs) being by far the most promising. In addition to turbine engines, CMCs also represent candidate materials for the control surfaces of potential hypersonic vehicles which will involve even more extreme temperatures approaching 1500 °C or more. The engineering challenges in developing these materials are further escalated by, for example, the need to design fine leading edges (radii as small as 1 mm) and integrated actively cooled walls for use along hypersonic flow paths, which can experience extremely high thermal gradients.[2]

Of the available CMC materials, textile composite structures with 3D woven carbon or SiC fibers embedded within a chemical vapor infiltrated SiC matrix demonstrate the best thermal and mechanical properties for these applications.[3–5] Weak interfaces, engineered using boron nitride (BN) or pyrolytic carbon coatings between the fibers and matrix, are used to enable fiber-bridging mechanisms for damage tolerance; the resulting difference in the strain to cause matrix and fiber failure imparts a degree of "ductility" which is otherwise absent in monolithic ceramics.[6–9] Owing to the complicated architectures of these materials, failure mechanisms are invariably complex, occurring at several length-scales in the form of, for example, matrix cracking, individual fiber breaks, fiber bundle or tow fractures, splitting cracks between individual fibers within tows, and delaminations between fiber tows. For these composites to reach sufficient maturity to be used as structural materials in such extreme temperature applications, it is crucial to develop a thorough quantitative understanding of the damage and failure mechanisms by observing their evolution under load in realistic service environments.

In contrast to the somewhat empirical experimental development of new materials in the past, the advent of integrated computational approaches to material design has shown great promise in materials evaluation using virtual testing and modeling; such approaches can essentially eliminate the vast number of experiments necessary to verify safe application of a material.[10–14] Computational models alone, however, are insufficient for such a task as it is vital to incorporate the appropriate physics describing the structural nature and length-scales of the materials in question and to fully quantify the damage processes under realistic temperatures and environments.

To this end, synchrotron radiation x-ray computed microtomography (μ-CT) is a powerful tool that provides 3D structural information non-destructively at relevant length-scales ranging from <1 μm to several millimeters.[15–21] Observing the time-dependent mechanical failure of the material in 3D in real time at high temperatures yields key parameters

a)Author to whom correspondence should be addressed. Electronic mail: roritchie@lbl.gov

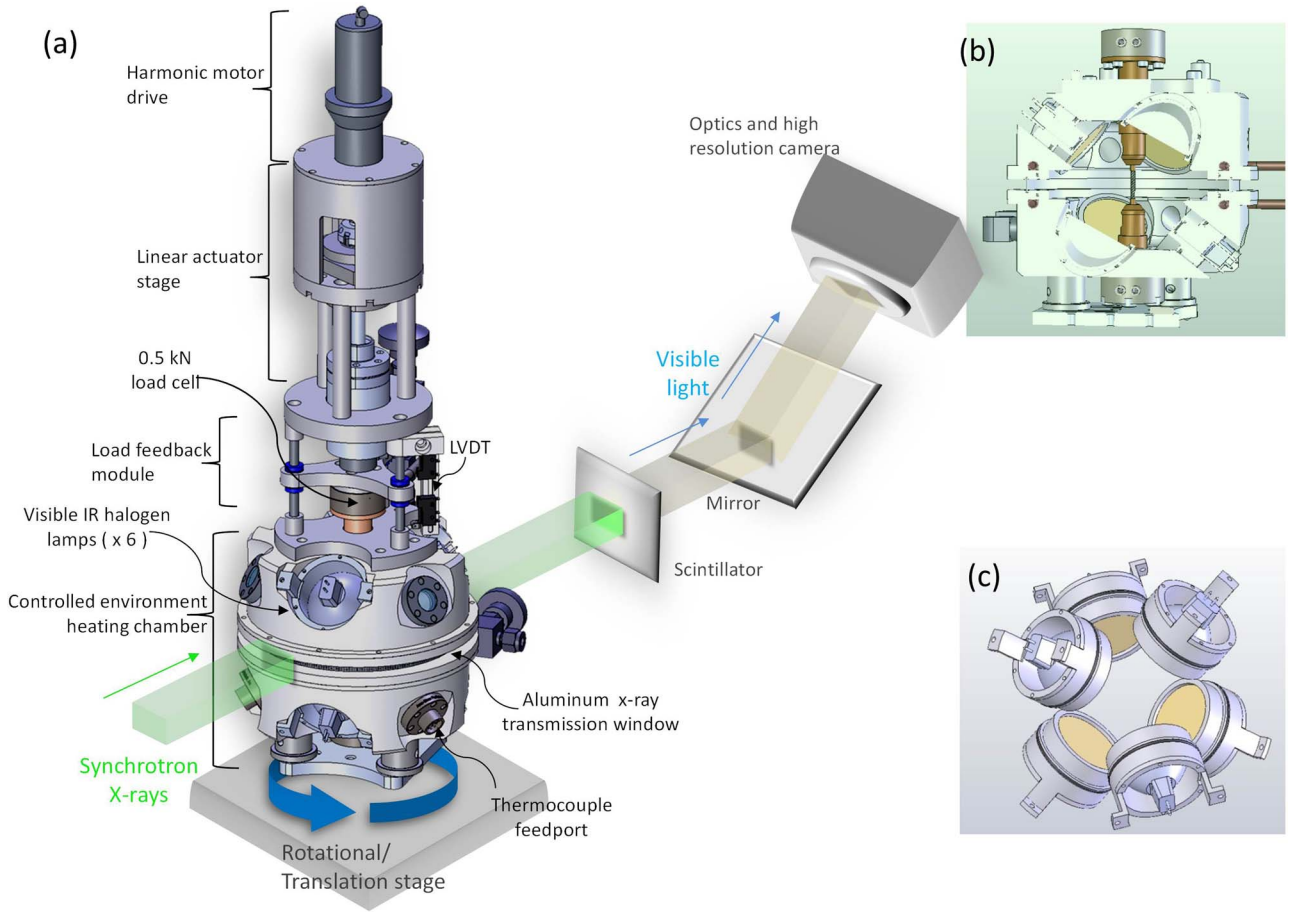

FIG. 1. (a) Schematic of *in situ* tension/compression test rig and imaging optics at tomography end station. X-ray projection intensities are converted to visible light by scintillator and imaged by magnifying lenses onto the camera. The deflecting mirror serves to move the camera out of the direct line of the beam to avoid potential damage from hard x-rays that pass through the scintillator. (b) Cross sectional view of heating chamber showing halogen heat lamps and test sample mounted in a pair of grips. (c) Positions of the six halogen lamps arranged around the chamber in a symmetrical confocal configuration.

required as input to models to allow for virtual material development and testing. Modern synchrotron-based CT imaging allows the required observations to be made with resolution down to several tenths of a micrometer,[22] while providing such high flux (orders of magnitude greater than available from laboratory-scale machines) that scan times for significant volumes of material can be held down to several minutes. Sub-micrometer resolution is essential to imaging single fibers,[22,23] allowing complete characterization of the fiber-scale microstructure,[24] as well as imaging critical damage events, many of which occur at the scale of a single fiber. Modest scan times are essential when studying materials at high temperature, to avoid large changes in the material due to creep or reactions, which would vitiate images.

The current paper presents details of a newly developed laboratory facility that is capable of reproducing the high temperatures, mechanical loads, and some of the gaseous environmental conditions encountered by structural components in service while simultaneously enabling us to take full advantage of high-resolution 3D imaging at a synchrotron beamline. First results from this work have been presented in Ref. 15. In this paper, we describe details of the device including the various procedural steps of the near-real-time x-ray micro-tomographic imaging of the sample during its failure process while at high temperature. The experimental capabilities and possibilities are demonstrated through 3D image data and analyzed results from tests conducted on two fiber-reinforced ceramic composite materials.

II. METHODS

A. Description of equipment

The *in situ* test rig integrates a heating/environmental-control chamber with a mechanical loading system as illustrated in Figure 1. The entire assembly is mounted on a portable high accuracy rotation stage, which can be inserted at the tomography end station on the hard x-ray tomography beamline (BL 8.3.2) at the Advanced Light Source at Berkeley.[25] 3D tomography images of samples undergoing simultaneous mechanical and thermal loading are obtained from sets of x-ray projection images (radiographs) recorded as the test instrument is rotated stepwise through an angular range of 180°. The radiographs are converted to visible light by a scintillator (Lutetium Aluminum Garnet) located at a distance of 125 mm from the sample, then recorded on a high-resolution, high-frame rate camera (pco.edge sCMOS camera, 2560 × 2160 pixels) after being imaged through an objective

lens system that allows convenient switching between different magnifications (10×, 5×, 2×, 1×). The pixel resolutions when using the 10× and the 5× lenses are 0.65 μm/pixel (field of view of 1.67 mm × 1.4 mm) and 1.3 μm/pixel (field of view of 3.28 mm × 2.8 mm), respectively. The projection images are used to reconstruct axial slices, which are stacked to generate a 3D volume.

The test sample is mounted in the center of a chamber (Fig. 1(b)), which serves as a mount for heating lamps (Fig. 1(c)), an enclosure for environmental control, and a support and reaction frame for the loading system. The walls of the chamber are equipped with an active cooling water jacket to maintain the walls and surrounding instrumentation at a stable low temperature (usually between 10 and 15 °C) while high temperature experiments are conducted. The chamber is sealed, and connected to a pumping system that can maintain a vacuum down to 10^{-3} Torr. Alternatively, controlled partial pressures of inert or reactive gas environments can be supplied by combined pumping and inflow of the chosen gas. The chamber is equipped with additional flanges for support equipment such as thermocouple connectors, vacuum gauges, gas inlet and outlet, and viewing ports.

1. Loading system

The loading system (Figure 1) is designed to deliver a maximum force of 2 kN in the vertical direction, along a line coincident with the rotation axis, to a test specimen held by a stationary grip near the bottom of the chamber and moving grip near the top of the chamber. The drive unit comprises a stepper motor with a compact 100:1 harmonic gear drive (ZSS 33-HD 08 Phytron) that drives a precision ball-screw driven linear slide resulting in a precise translational motion with a minimum incremental step of 0.1 μm. A load cell is located between the top specimen grip and the drive unit (LCFA-1K Omega Eng. Inc.; 0.5 kN maximum load, ±0.5 N repeatability). Displacement measurements are provided by a linear variable differential transformer (LVDT; Macrosensors, BBPM-375-200, 0.4 μm repeatability) attached between the linear slide and the wall of the chamber.

2. Mounting and alignment for tomography

Precise alignment of the sample with the rotation axis and stability of the rotation axis itself while running a tomography scan are critical for avoiding artifacts in reconstructed data. Sample displacements must typically be less than 0.1 μm. This is particularly challenging since the rig is connected to several supply lines providing power to the motor, lamps, and other instrumentation, along with chilled water and vacuum lines in and out of the rig. The entire system with the connections rotates 180° around a central axis on an air-bearing rotation/translation stage. Kinematic mounts installed at the base of the rig assist in a quick, precise, and rigid installation of the rig. The base connects to its counterpart as part of a magnetic table enabling automated translational alignment of the rig. Alignment is achieved by monitoring the position of the sample in radiography as the rig is rotated through 180°.

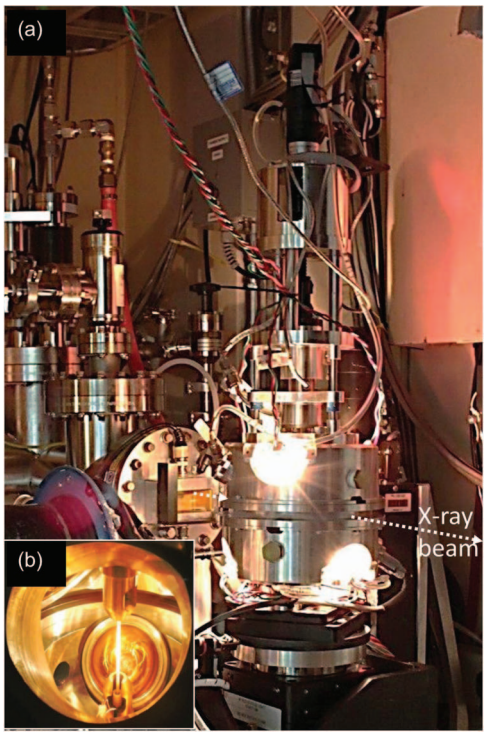

FIG. 2. (a) High temperature *in situ* test rig in operation at the x-ray microtomography beamline, at the Advanced Light Source. (b) SiC sample inside the heating chamber, held between two grips, under tensile load at 1000 °C.

3. Specimen heating

Sample heating is accomplished with six 150 W infrared halogen lamps fitted with gold ellipsoidal reflectors (L6409, 25 V, 150 W, focal length 44 mm, International Light Technologies, Inc.), mounted symmetrically in the chamber wall in a confocal configuration (Fig. 1(c)).[26,27] The positions of the lamps (distance from center of chamber) are adjustable to allow some variation of the focused size of the hot zone in the center of the chamber. The lamps are operated simultaneously, and controlled using a programmable power supply (ZUP, 21 V, 21 A, 430 W, TDK-Lambda). Images of the rig in operation with the sample being heated *in situ* are shown in Fig. 2. In the most highly focused condition the region of high heat flux is approximately spherical with diameter ∼5 mm. In this condition, specimen temperatures up to 2300 °C have been achieved using the types of specimen described in Sec. II B. In the defocused condition, specimen temperatures of 1500 °C have been achieved over a specimen length of ∼8 mm.

4. X-ray transmission window

The chamber incorporates a cylindrical x-ray transmission window fabricated from an aluminum alloy (Al-Mg-Si alloy 6061-T6) with thickness 300 μm, height 7 mm, and diameter 150 mm, which connects the upper and lower halves of the chamber (Fig. 1). The window performs the dual roles of allowing minimally obstructed transmission of the x-ray beam into and out of the chamber as the chamber is rotated through 180°, while providing mechanical support for both

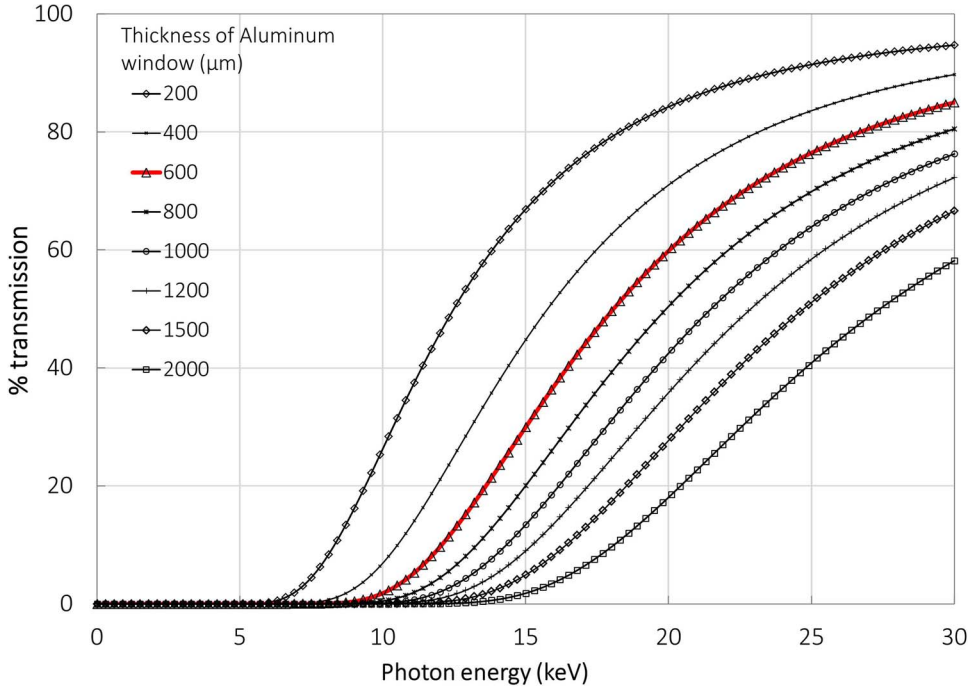

FIG. 3. Plot of transmission efficiency as a function of x-ray energy for various path lengths through an aluminum window.

the weight of the rig hardware above the window and for reaction of the forces applied to the test specimen. The window thickness was designed as a compromise between requirements of these two roles (minimal thickness for x-ray transmission versus maximum thickness for mechanical strength). Finite element structural analysis indicated that a wall with these dimensions can support the required loads for experiments in which tensile forces up to 2 kN are applied to the test specimen.

The dependence of x-ray transmission on thickness and x-ray energy is shown in Fig. 3. For white light, in the energy range 11–45 keV, the x-ray transmission for a 300 μm thick window (600 μm path length) is 6%–80%. Previous x-ray beam characterization and parametric studies of the tomography procedure at beamline 8.3.2 have indicated that a minimum average bright-field count up to 16 000 photons on the projected image is needed to yield reconstructed data without noticeable noise. With previously published calibration of the x-ray flux over this energy range,[25] this count requires exposure times per projection of 50 ms for white light in the energy range 11–45 keV, or 1 s for monochromatic light of energy 30 keV, when using the 300 μm window. A typical 3D scan consists of 1025 radiographs, requiring total scan times of 3 min for white light mode and 28 min for monochromatic light. Owing to the significantly shorter scan time, most of the tomography scans were conducted in white light mode.

B. Sample preparation and test procedures

1. Test specimens and loading fixture

Two types of composite samples were prepared for the *in situ* testing—one was in the form of unidirectional reinforced rods (~1 mm diameter, 55 mm length) consisting of a single tow of SiC fibers (Nippon Carbon Hi-Nicalon Type-S, 500 fibers/tow, fiber diameter 12 μm) embedded within a matrix of SiC formed by chemical-vapor infiltration (CVI). The other was in the shape of beams (2 mm × 3 mm × 55 mm) cut from a plate of textile-based composite consisting of a woven preform of carbon fiber tows (angle interlock weave structure, T300 carbon fibers, 6000 fibers/tow, fiber diameter 7 μm) embedded in a matrix of SiC formed by a combination of CVI and infiltration/pyrolysis of a slurry of SiC particles in a polymer precursor for SiC.[15] The fibers within each composite were surrounded by thin weak interphases of thickness 0.5–2 μm; boron nitride in the SiC_f-SiC_m composite, and pyrolytic carbon in the C_f-SiC_m composite.

Customized grips were developed to suit the specimen and the conditions of testing. For high temperature tests on ceramic composites, the specimens were bonded into molybdenum end fittings, which were then connected to the loading system via the ball-and-socket system illustrated in Fig. 4. The bonding of the end fittings was achieved using the same polymer precursor used in the matrix, which decomposes at high temperature to form a strong SiC bond. The choice of molybdenum was based on the need to match the coefficient of thermal expansion of the composite specimen as well as to survive the pyrolysis heat treatment. The specimen gauge length between the molybdenum end grips was 15 mm, consistent with the height of the transmission window (7 mm) and the size of the hot zone (~5 mm diameter). The specimen cross section dimensions are in general limited by the hotspot size, requirements for spatial resolution (micrometer/pixel), maximum failure stress, and x-ray attenuation by the sample. In the experiments reported here the cross-section dimensions were limited to no more than 2 mm in order to allow optimal imaging at high resolution (0.65 or 1.3 μm)

The molybdenum ends were threaded into stainless steel balls which seated into spherical sockets of the loading grips

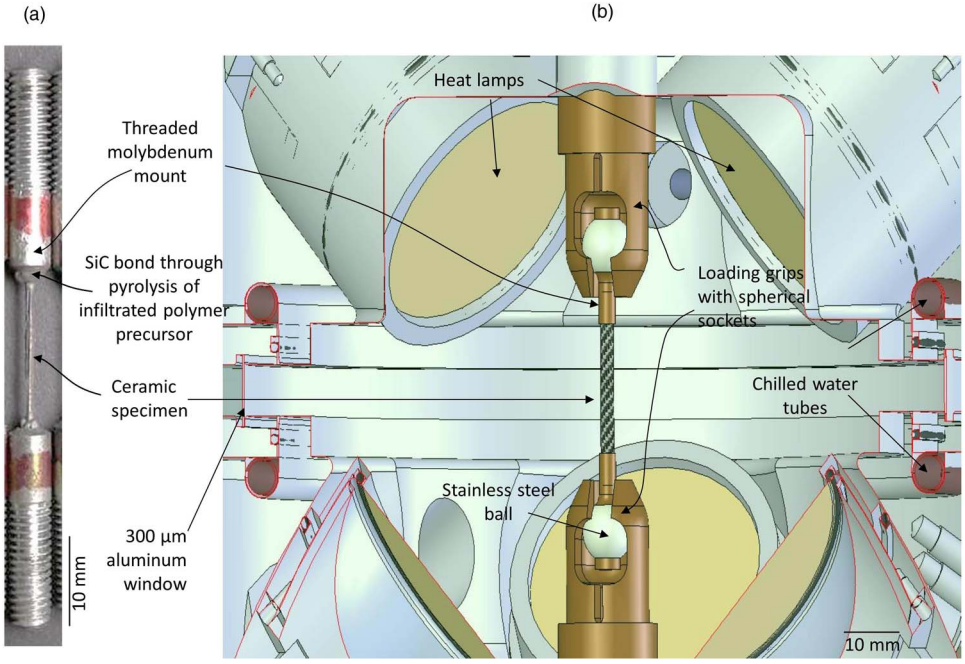

FIG. 4. Schematic illustrations showing: (a) test specimen with end fittings and (b) specimen mounted between upper and lower grips.

(Fig. 4.). The sockets were machined from phosphor-bronze, which was chosen for its combination of mechanical strength, relatively high thermal conductivity (to minimize the grip temperature), relatively high melting point, and easy machinability. The ball-socket geometry of the grips provides a self-aligning system that minimizes bending moments, thus ensuring a pure tensile load. The test specimen, with the threaded balls attached to the ends, was inserted into the grips through one of the lamp sockets.

2. Data acquisition and rig control

A dedicated data acquisition and control system developed on the National Instruments Labview platform is used to operate the rig remotely (the test rig and rotation stage being housed in a lead–shielded hutch). The control system consists of power drives and a motion controller system (NI-PXI-7340, National Instruments Corporation, Austin, TX) that remotely control the loading system and the lamps. The data acquisition system receives input from the load cell, motor encoder, linear variable differential transformer, pyrometer, pressure gauges, and a precision gas flow controller. The software interface interacts with both the control system and acquisition system providing a flexible programming environment to customize the operation of the rig for monotonic or cyclic variation of mechanical load or temperature. The rig is operational in either displacement-controlled or load-controlled mode.

3. In situ micro-tomography scans

Before and after each scan, a set of images is collected for background calibration. These include both bright-field images (exposures without sample in the x-ray path) and dark-field images (exposure with the x-rays blocked, to correct for any stray light). The current translation stage has a limited range of motion that is not sufficient to move the entire chamber out of the beam. Consequently the bright-field images are taken with the stage moved sufficiently to remove the test specimen from the beam but with the aluminum window remaining in the x-ray path. Although not ideal, these bright-field images have been shown to provide satisfactory background correction, with no noticeable artifacts in the reconstructed slices.

Over a single tomography scan, 1025 projection images are recorded. The images are processed in a sequence of steps that include background normalization (compensates for change in energy over a scan) and background subtraction (compensates for dust, scratches, and defects on the scintillator). For samples longer than the height of the field of view, multiple scans collected with the sample displaced in steps in the vertical direction are tiled together. Sinogram images are generated from the corrected images, which basically consist of a 2D array of information pertaining to the absorption along the x-ray path at each angular position of the sample. The sinograms are processed using a filtered back projection algorithm to generate the reconstructed tomography slices using the reconstruction software package-Octopus (inCT, Universiteit Gent, Gentsesteenweg, 9300 Aalst, Belgium).[28] Data were visualized and analyzed in Avizo 6.1 (VSG, Visualization Sciences Group, Inc., Burlington, MA) and ImageJ (Rasband, W.S., ImageJ, US National Institutes of Health, Bethesda, http://imagej.nih.gov/ij/).[29]

Typically, a reference 3D scan of the test specimen is acquired at the beginning of a test, with a very small preload (5 N) applied to the specimen to ensure there is no movement of the specimen during the scan. Then the prescribed load and temperature cycles are undertaken with hold points at selected times to allow further 3D scans. It is currently not feasible to monitor a test using real-time

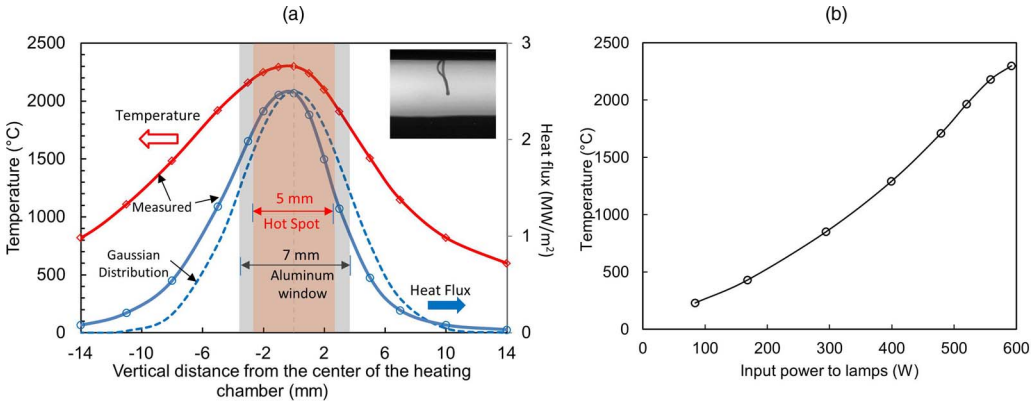

FIG. 5. (a) Distributions of temperature measured by bare thermocouple (red) and calculated heat flux (blue) along vertical axis of chamber. Measurements obtained by moving the thermocouple tip while continuously monitoring position by radiography (inset). Heat flux calculated from measured temperatures using Eq. (1). Gaussian heat flux (broken curve) shown for reference: $\dot{q}_L = \dot{q}_o \exp\left[-(x/d)^2\right]$ with $d = 5$ mm. (b) Temperature measured by bare thermocouple at the center of the chamber as a function of power supplied to heating lamps.

feedback from the 3D tomography images, since the process of generating the final reconstructed slices requires about 90 min of computational processing time. (This likely will be reduced as new computational facilities come on line.) However, in some cases it is possible to monitor the presence of damage directly from radiographs taken as the load is increased incrementally and use this information to determine the points at which full 3D scans are acquired. Also, in some cases the cracks detected in radiography are accompanied by a small drop in the load measured by the load cell.

C. Temperature measurements

Accurate measurement of high temperatures within the CT environment is challenging because a sensor, such as a thermocouple, cannot be inserted in the x-ray beam, where it would interfere with x-ray imaging. The temperature must therefore be inferred indirectly from remote observations, made either by thermocouples sited away from the imaged portion of the specimen or by radiation measurements made from outside the heated chamber using focusing optics. However, both of these approaches have limitations in this environment, as discussed below. Therefore, several approaches were employed to develop a measurement method that yields testable results.

The temperature of the central hot region of a test specimen under given operating conditions of the heat lamps is dependent on the balance of the following heat flow in and out of the specimen:

(i) radiative heat absorbed by the specimen (dependent on absorptivity of specimen and incident heat flux);
(ii) heat radiated from the hot surface of the test specimen to the cooled chamber walls (dependent on specimen surface temperature and emissivity);
(iii) heat loss by conduction along the test specimen towards the cooled grips (dependent on temperature gradient along the specimen and on the product of the specimen diameter and conductivity as well as thermal impedance in the grip region);
(iv) heat loss by convection from the surface of the test specimen to a surrounding gas.

An approximate analysis indicates that the conduction along the specimen to the grips has a significant effect. For the SiC test specimens discussed below (with diameter 1 mm and thermal conductivity 20 W/m K) at 1700 °C, the reduction in specimen temperature due to conduction towards the grips is estimated to be in the range 150–250 °C. The reduction due to convection in an ambient gas should be smaller (less than 25 °C).

Given that the conductive heat loss influences the specimen temperature significantly and the fact that *in situ* temperature measurement by direct attachment of thermocouples to each test specimen is not feasible (because of shadowing of the x-ray beam and the small size of specimens), the following approaches for measuring and calibrating specimen temperatures were investigated.

1. Thermocouple measurements

The distribution of radiation heat flux incident on the test specimens was calibrated by inserting a bare thermocouple (Type C, W/Re thermocouple; Model No. T5R-005-12, Omega Engineering, Inc.) in place of the test specimen. The thermocouple was attached to the top movable grip via a standard insulating alumina thermocouple tube and translated along the vertical axis of the hot zone while monitoring its position visually by radiography (with the chamber under 10^{-3} Torr vacuum). With the lamps operating at a total power of 560 W, the resulting measured temperatures are shown in Fig. 5(a). The dependence of the temperature measured at the center of the hot zone with lamp power is shown in Fig. 5(b). With the system running continuously over a 48 h period, the temperature remained stable within 2% (±40 °C).

Since the thermocouple was thermally insulated from the cooled grips it is reasonable to assume that heat flow along the thermocouple is negligible. In this case, the thermocouple temperature, T, is determined by radiation equilibrium, i.e., by equating the absorbed heat flux ($\dot{q}_a = \varepsilon_a \dot{q}_L$, where $\dot{q}_L$ is the incident radiation heat flux and ε_a is the absorptivity)

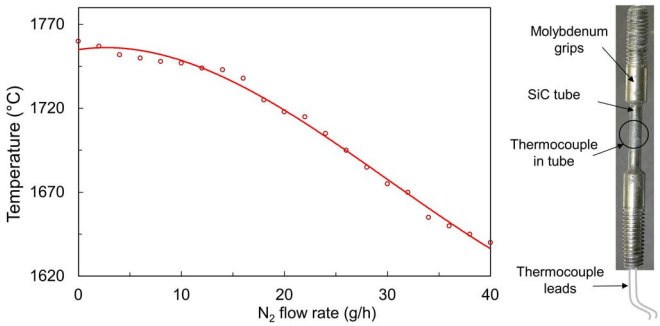

FIG. 6. Variation of specimen temperature with flow rate of nitrogen into the heating chamber. Temperatures measured by C-type thermocouple inside cylindrical SiC calibration specimen at input power of 592 W.

to the heat flux radiated from the hot surface ($\dot{q}_r = \varepsilon\ \sigma\ T^4$, where ε is the emissivity and σ the Stefan-Boltzmann constant). If we assume that the thermocouple acts as a grey body, the absorptivity is equal to the emissivity and the measured temperature is related directly to the incident heat flux:

$$\dot{q}_L = \sigma\ T^4. \tag{1}$$

The incident heat flux calculated from Eq. (1) is plotted in Fig. 5(a). In the central region, the heat flux is closely approximated by a Gaussian distribution (broken curve) with characteristic width $d = 5$ mm. This represents the width of the temperature region that encompasses the maximum thermocouple temperature minus ~10%.

2. Embedded thermocouple measurements

A calibration specimen containing an embedded thermocouple was constructed to allow measurement of typical magnitudes of the effects of axial conduction and convection. The calibration specimen (Fig. 6) consisted of a tube of sintered monolithic SiC (2.5 mm OD and 1.6 mm ID) with dimensions (length and cross-sectional area) similar to those of the test specimens and mounted into the test fixture in an identical manner, so that effects of emissivity, convection, and conduction are similar. A type-C thermocouple was located inside the tube, at the mid-point of the specimen. At a lamp power setting of 592 W and a vacuum environment (10^{-3} Torr), the temperature measured was 1760 °C, which is 220 °C lower than the temperature recorded by the bare thermocouple under identical conditions (Fig. 5(b)).

Most testing was performed with combined pumping and inflow of a gas supplied at a controlled flow rate for control of environment (ultra-high purity nitrogen or argon for inert environment, oxygen or mixed O_2/N_2 for oxidation studies). The effect of gas flow rate on the temperature measured using the calibration specimen with a lamp power of 592 W is shown in Fig. 6. For flow rates above 10 g/h, the temperature decreases almost linearly with increasing flow rate, by as much as 120 °C at a flow rate of 40 g/h. Most testing was done with a flow rate of 20 g/h, for which the temperature drop due to convection is about 50 °C.

3. Pyrometry measurements

Pyrometry techniques that make use of the known form of the temperature dependence of the spectral intensity of thermal radiation emitted from a surface are capable of providing very accurate remote measurements of surface temperatures and are an especially convenient approach when the temperatures are high. However, errors are introduced when the heating of the test sample is provided by radiation. In this case, the radiation collected by the pyrometer includes a fraction of the source radiation that is reflected from the test surface as well as the thermal radiation emitted from the test surface. For a diffusely reflecting grey surface, the ratio of the intensities of the reflected and emitted radiation is $(1 - \varepsilon)/\varepsilon$, where ε is the emissivity. For SiC materials, in which the high-temperature emissivity is typically in the range 0.85–0.95, this ratio is 0.05–0.17. The resulting error in the temperature inferred from the pyrometer measurement is dependent on the difference in the temperatures of the heating lamp and the test surface. In the present experiments this error was characterized by cross referencing the pyrometry result with the embedded thermocouple measurements as described below.

The temperatures of the test specimens were measured using a full-spectrum pyrometry technique, in which the radiation emerging from the test surface is sensed by a probe consisting of an achromatic lens (25 mm diameter, 100 mm focal length) that projects an image of the heated zone of the sample (1:1 magnification) onto the end of a 200 μm diameter optical fiber connected to a spectrometer (200–1100 nm detector range, Ocean Optics USB 4000, Ocean Optics, Dunedin, FL). The probe is mounted externally on the rig and oriented to point directly at the center of the hot spot through one of the viewports (borosilicate glass with 92% transmission in the wavelength range 350–2200 nm, Corning 7056, 1.33 CF Flange Accu-glass Products Inc.). The 1:1 focusing optics and small fiber optic diameter ensure that only radiation originating from a small uniform hot central area of the 2 mm wide test specimen is sampled. The system can operate at an acquisition rate of 4 ms per spectrum, thus allowing the tracking of temperature changes over small time steps.

The spectral intensity, $R(\lambda, T)$, of radiation emitted from a surface with emissivity ε at temperature T is given by Planck's law:

$$R(\lambda, T) = \frac{2\varepsilon\, h\, c^2}{\lambda^5}\left[e^{\frac{hc}{\lambda kT}} - 1\right]^{-1}, \tag{2}$$

where λ is the wavelength, c is the speed of light, and h and k are the universal Planck and Boltzmann constants. For the detector wavelength range used below (680–760 nm) at the temperatures of interest (>1000 K), we have $\exp(hc/\lambda kT) \gg 10^{10} \gg 1$ and Eq. (2) simplifies to a convenient form (Wien approximation)

$$R(\lambda, T) = \frac{2\varepsilon\, h\, c^2}{\lambda^5} e^{-\frac{hc}{\lambda kT}} \tag{3}$$

or

$$\ln\left(\frac{R(\lambda, T)\,\lambda^5}{2\,h\,c^2}\right) = -\left(\frac{hc}{\lambda k}\right)\frac{1}{T} + \ln\varepsilon, \tag{4}$$

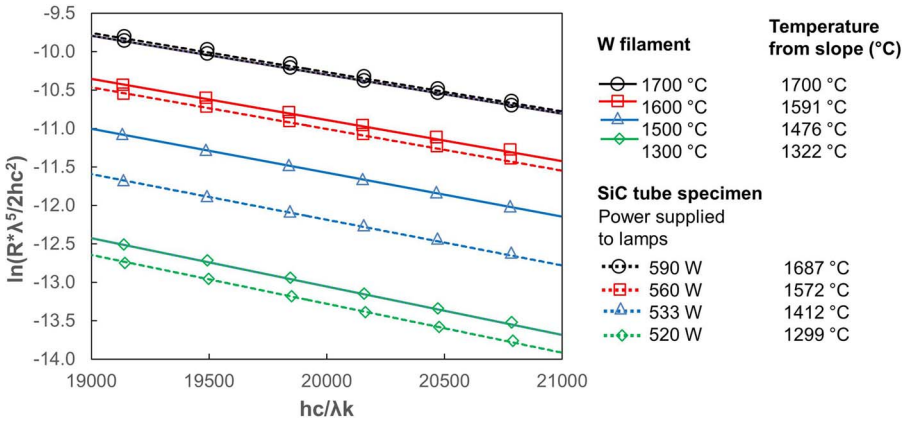

FIG. 7. Spectral intensities, $R(\lambda)$, obtained from pyrometer measurements calibrated with reference tungsten ribbon filament at a temperature of 1700 °C, plotted in accord with Eq. (4) for the wavelength range 680–760 nm. Results as indicated for tungsten filament at several other known temperatures and for SiC tube specimen while being heated by the lamps at several power levels. Temperatures evaluated from the slopes of the plots are indicated.

where if the spectral intensity is measured as a function of λ at fixed temperature and plotted as $\ln(\frac{R(\lambda,T)\lambda^5}{2hc^2})$ versus $(\frac{hc}{\lambda k})$, the temperature is given by the reciprocal of the slope and the emissivity is given by the intercept.

The output of the detector was calibrated using a reference tungsten ribbon filament lamp (model STL-H, Pyrometer Instrument Co, Windsor, NJ) with known temperature-current relation. The tungsten filament, which is 2.6 mm wide, was placed at the same distance from the lens as the sample. The calibration involves measuring the detector output $I(\lambda, T_{ref})$ as a function of wavelength at a reference filament temperature T_{ref} and calculating the ratio of the output to the spectral intensity $R(\lambda, T_{ref})$ given by Eq. (3). This ratio is then used to convert the measured output of the detector to the spectral intensity for measurements on test specimens of unknown temperature. This procedure assumes that the wavelength dependence of the ratio $I(\lambda, T_{test})/R(\lambda, T_{test})$ is insensitive to the test temperature T_{test} over the range of wavelengths used for the measurement. In practice this is a reasonable approximation for a limited range of test temperatures around T_{ref}. In the current tests, the calibration was carried out with the tungsten filament at $T_{ref} = 1700$ °C over the wavelength range 680–760 nm. Then the detector was used with this calibration to measure the temperature of the tungsten filament operating under a different current and thus at a different temperature (T_{test}, known). Comparison of the measured and known values provides an estimate of the accuracy of the measurement at the temperature T_{test}. Results of these measurements at $T_{test} = 1300$, 1500, and1600 °C are shown in Fig. 7, plotted in accord with Eq. (4). Over this temperature range, the calibration is accurate within ±25 °C.

Also shown in Fig. 7 are results of pyrometry measurements from the SiC calibration specimen discussed above (with embedded thermocouple) while being heated by the lamps at several different power settings that produced temperatures in the same range. The temperatures obtained from these measurements are compared with simultaneous direct measurements from the embedded thermocouple in Fig. 8. The two measurements agree within 40 °C over the temperature range 1300–1700 °C.

In summary, the uncertainty in the measurement of a single temperature, T, is approximately ±20 °C over the temperature range 1300–1700 °C when the temperature is inferred from the measured radiation flux from the specimen and a calibrating radiation measurement made using a reference tungsten filament lamp. The uncertainty in the change in temperature, δT, when the heat flux of the heating lamps is increased or decreased is expected to be much smaller, ±2 °C, for a range of $\delta T \leq 200$ °C.

III. *IN SITU* TEST RESULTS AND DISCUSSION

Having established a procedure to subject test specimens to tensile/compressive load at high temperature in a controlled gas environment, while continuously monitoring all the parameters, we applied the technique to observe the development of damage in the two ceramic composite materials described above, while they were loaded to failure. The SiC–SiC "mini-composite" specimens, with diameter approximately 1 mm, allowed assessment of the quality of image data at the highest magnification/resolution (0.65 μm/pixel), where the image quality is most sensitive to phase contrast effects and sample movement (thermal/mechanical stability of the

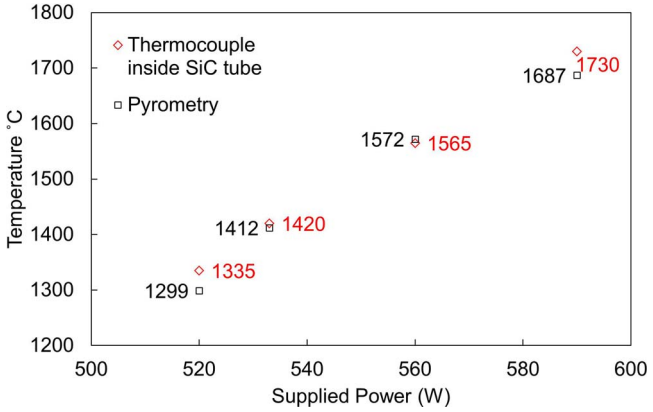

FIG. 8. (a) Comparison of temperatures measured at the center of the SiC calibration sample using pyrometry and the embedded thermocouple at different power settings.

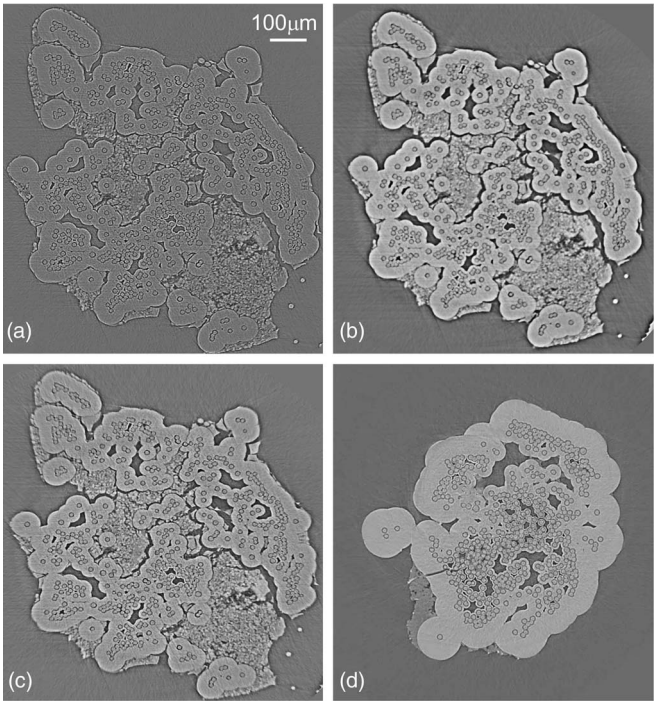

FIG. 9. Cross-section images of SiC-SiC mini-composites, processed using the (a) filtered back projection algorithm (FBP), (b) Modified Bronnikov Algorithm (MBA), and (c) Bronnikov Assisted Correction (BAC) algorithms for reconstruction of data acquired using 30 keV monochromatic light. Small dark circles are the BN coatings surrounding the fibers. The MBA step in (b) boosts the contrast between different phases in the sample but also introduces some degree of blurring of the edges. The BAC step in (c) corrects for blurring and maintains the contrast achieved in (b). (d) BAC-processed image for white light data (collected from a different sample of the same type of composite) showing superior image quality with reduced noise and reduced phase-contrast artifacts.

test rig). The textile-based C-SiC composite investigated at 1.3 μm/pixel resolution allowed study of interactions of cracking damage with a more complex reinforcement architecture.

A. Quality of reconstructed images

In high-magnification/high-resolution images, phase contrast effects are significant owing to the 125 mm sample to scintillator propagation distance. An example is seen in Fig. 9(a), which shows a transverse cross-section of the SiC-SiC mini-composite specimen, with phase contrast effects evident as the bright/dark Fresnel fringes around the perimeter of the composite and around the edges of the internal voids. Although this makes some image features more readily visible and results in seemingly sharpened radiographs, it induces erroneous values, artifacts, and loss of resolution in the CT reconstruction. For low absorbing materials, the Modified Bronnikov Algorithm (MBA) and its extension, the Bronnikov Assisted Correction (BAC) are effective in significantly reducing phase contrast artifacts when applied to images reconstructed using the usual filtered back-projection algorithm (FBP).[30,31] For the ceramic composite materials, which have higher x-ray absorption (close to 40%), these algorithms are expected to be less effective (the MBA and BAC algorithms are typically implemented on projection images collected with a near 100% transmission).

Images from the SiC-SiC mini-composite specimen collected in both monochromatic and white light conditions and processed using FBP, MBA, and BAC are compared in Figs. 9(a)–9(d). In all cases, the fibers and the BN coatings are visible. Processing with the MBA (Fig. 9(b)) reduces high frequency noise and increases contrast between phases, but also produces undesirable smoothing of sharp edges. This smoothing is removed by further processing with the BAC (Figs. 9(c) and 9(d)). Phase contrast is evident in all cases, although it is significantly reduced after processing with the BAC (Figs. 9(c) and 9(d)), especially in the case of the white light image (Fig. 9(d)). The signal-to-noise ratio is much higher for the white light image than for the monochromatic light image, owing to the much higher photon flux ($\times$100).

B. Damage evolution in single-tow composite

Selected observations are shown in Fig. 10 of damage developing during loading of two SiC-SiC minicomposite specimens in uniaxial tension, one at room temperature and the other at 1750 °C, both in an inert environment (nitrogen). The force-displacement responses are shown in Fig. 10(h). The forces were increased under displacement control at a constant rate of 0.5 μm/s, with hold points as indicated, where the tomography data were acquired.

Longitudinal slices from the 3D tomographs obtained at three of these hold points for each specimen are shown in Figs. 10(a)–10(f). The image quality, as judged in terms of pixel noise, contrast, and resolution, was identical in images collected at room temperature and high temperature (all were processed with BAC as described above). We note that in the longitudinal slices the individual fibers and coatings are not all clearly distinguished as they are in the transverse slices (Fig. 9) for two reasons: the thickness of the slices (0.65 μm) is sufficiently large that in regions where the fibers are closely packed some overlap of adjacent fibers and coatings occurs; also the alignment of the fibers is not perfect so that some fibers move in and out of the slice over the height of the images.

Two types of damage are visible in the images of Figs. 10(a)–10(f): cracks in the matrix oriented approximately normal to the applied force (and the fibers), and fractures of individual fibers at locations that do not coincide with the matrix cracks. The matrix cracks extend across the entire cross-section of the test specimen, while remaining bridged by intact fibers, as can be seen clearly in many regions. The crack bridging response is responsible for the tough behavior of these composites and is enabled by the weak layer of BN surrounding the fibers, which allows debonding and frictional sliding.[7–9] The locations and loads at which individual fibers fracture are dependent on the statistical distribution of flaws in the fibers and the magnitude of the frictional sliding stress. These are the key constitutive properties dictating the macroscopic stress-strain response of the composite that are needed as input for models that predict mechanical performance and lifetimes.[3,7,10]

From Figs. 10(a)–10(f), it is evident that the opening displacements of the matrix cracks increase as the applied loads increase, while the opening displacements at given load are

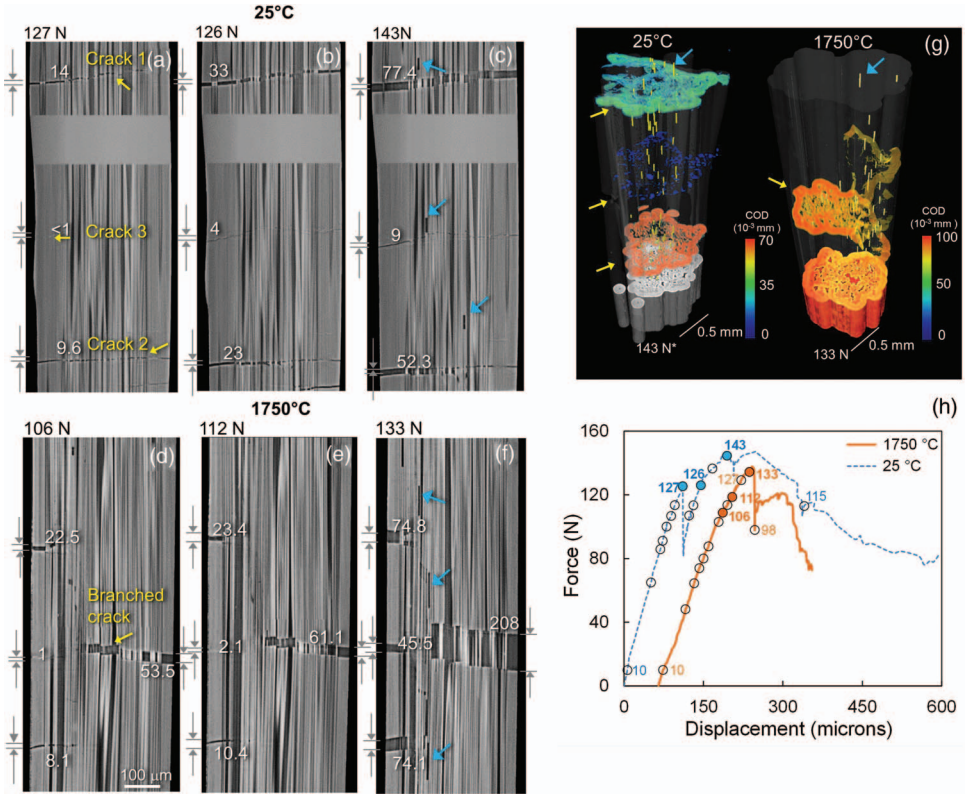

FIG. 10. *In situ* testing of single-tow SiC–SiC mini-composite specimens at low and high temperatures (25 °C and 1750 °C). (a)–(f) Axial tomographic slices obtained from reconstructed data show evolution of cracks in the composite specimens at three stages of loading. Yellow arrows indicate cracks in the SiC matrix, which open with increased load. Blue arrows in (c) and (f) point to gaps where individual fibers have broken and pulled apart. (Horizontal featureless grey region in (a), (b), and (c) is missing data due to lack of a tiled scan.) (g) 3D visualization of matrix cracks and fiber breaks for the two specimens under the loads indicated. Adapted from Ref. 13. (h) Force–displacement curves from tests of (a)–(f). Red curve offset by 70 μm for visual clarity. Hollow circles indicate loads at which μ-CT data were acquired; blue and red solid circles indicate loads corresponding to images in (a)–(f).

larger at high temperature than at low temperature. These displacements have been measured and used in conjunction with micromechanical models to calculate the frictional sliding stress between the matrix and fibers.[15] In this case, the frictional stress is 2 MPa at room temperature and 0.4 MPa at 1750 °C. These values are also consistent with the sliding distances observed between the matching ends of individual fractured fibers. The decrease in sliding resistance at high temperature has been attributed to changes in the structure of the BN layer at high temperature.[15]

The 3D datasets contain comprehensive information of the entire sequence of damage events and their evolution that are difficult to illustrate fully in 2D image slices. An alternative 3D visualization of the spatial distribution of damage at a load near the peak in the load-displacement curve for each of the tests is shown in Fig. 10(g). In these images the matrix cracks and fiber breaks have been marked with a color code that indicates the crack opening displacement, while the matrix and fibers have been rendered almost transparent. An appreciation of the temporal development of the damage as the load increases can be gained by assembling a set of such images to form a video. Such representations of damage are key to being able to extract the maximum information from the large amount of data collected in this type of tomography experiment. In this case this was done mainly by manual searching through the 3D tomography image to identify and mark the damage features (attempts to use existing automated image analysis software to do this met with limited success). Future adaptations of image recognition software to automate this process would be a major advance.

The accuracy of the measured crack opening displacements is dependent upon the edge resolution in images such as Figs. 10(a)–10(f). As shown in Fig. 11, the edge of the matrix crack appears in the image as a pair of bright/dark phase-contrast fringes with separation of ~10 μm. In our measurements, the location of the edge was taken as the position corresponding to the mid-point of the grey levels between the bright and dark fringes. This position did not change significantly when the FBP images were further processed by MBA and BAC, even though the widths and intensities of the fringes changed. The resulting uncertainty in the edge position (estimated at ± 3 μm) places a limit on the accuracy of the absolute crack opening displacement that can be measured from an individual image. However, in a series of images such as Figure 10, in which the edge contrast is identical in all the images, the incremental opening of a crack between two images obtained at different applied loads can be measured with accuracy an order of magnitude higher, as long as the crack opening is sufficiently large that fringes from opposing crack surfaces do not overlap. Overlap begins to occur for crack opening smaller than 10 μm. For smaller crack openings, the crack appears in the image as a dark feature with width that does not represent the opening displacement.

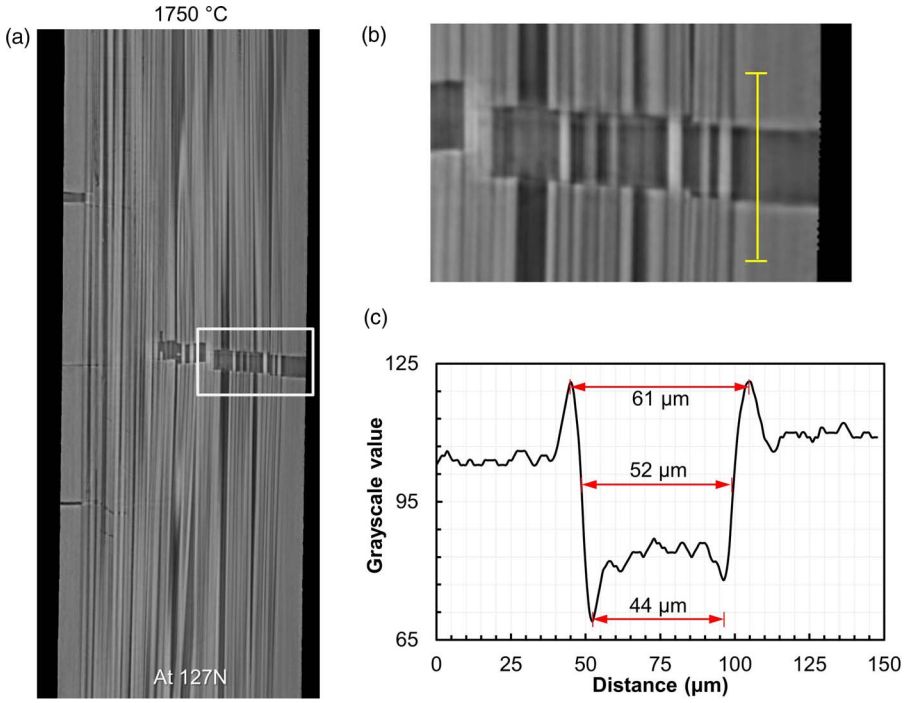

FIG. 11. (a) and (b) Higher magnification images from high-temperature test in Fig. 10, showing detail of edge contrast at matrix crack that is bridged by fibers. (c) Plot of grey level along line shown in (b).

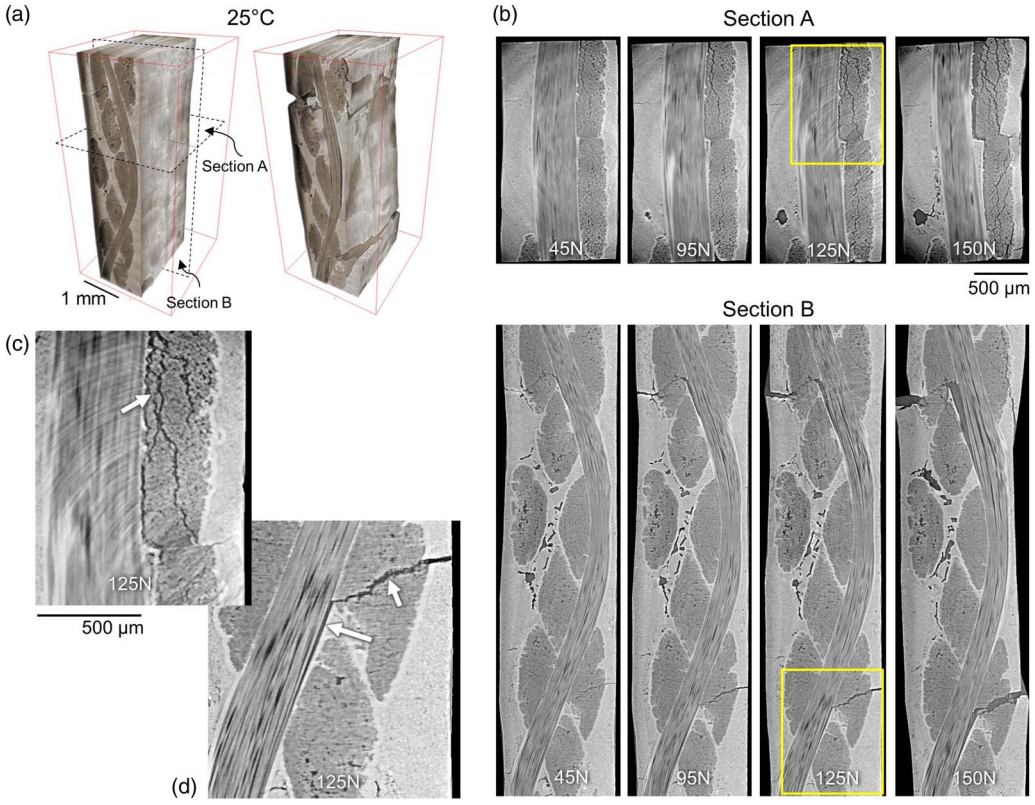

FIG. 12. *In situ* tomography of C–SiC composite with textile-based carbon fiber reinforcements under a tensile load at room temperature. (a) 3D visualization showing damage on exterior surfaces. (b) Sequences of images from transverse and axial slices (sections A and B) showing evolution of internal damage with increasing applied load. (c) Enlargement from area indicated in transverse slice at 120 N load, showing splitting cracks in an axial tow. (d) Enlargement from area indicated in axial slice at 120 N load, showing transverse crack that extended from surface through a transverse tow and deflected at underlying axial tow causing splitting of the tow. Splitting damage in axial tow is visible in (c) but is masked by other contrast interference effects in (d).

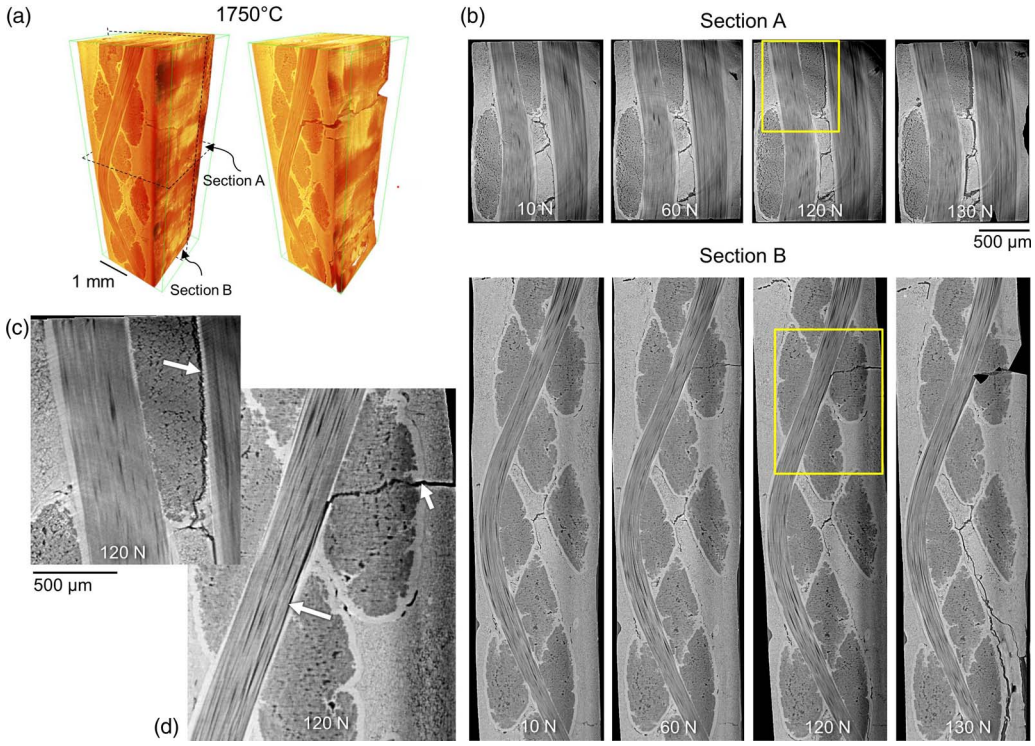

FIG. 13. *In situ* tomography of C–SiC composite with textile-based carbon fiber reinforcements under a tensile load at high temperature (1750 °C). (a) 3D visualization showing damage on exterior surfaces. (b) Sequences of images from transverse and axial slices (sections A and B) showing evolution of internal damage with increasing applied load. (c) Enlargement from area indicated in transverse slice at 120 N load, showing deflected crack at edge of an axial tow. (d) Enlargement from area indicated in axial slice at 120 N load, showing transverse crack that extended from surface through a transverse tow and deflected at underlying axial tow.

More generally, the limitation due to interference fringes in the transmitted x-ray intensity can be avoided if incremental displacements of features are measured using digital image correlation (DIC) techniques. The DIC method exploits any source of contrast that is available in the material and is distributed throughout its volume. The contrast source may occur either naturally or by the addition of contrasting fine particles. The DIC method uses correlation integrals to detect relative displacement of the contrast features, e.g., when the external load is increased. Analysis of discontinuities in the displacement field at cracks allows the inference of the absolute crack displacement far more accurately than is possible using a single image of the crack. This advantage in 3D CT image analysis is analogous to the advantage of DIC in analyzing 2D images acquired by conventional means. In application to CT images, the DIC method has yielded crack displacements with an accuracy of less than 1 μm.[22]

C. Damage evolution in textile composite

Observations of damage developing during similar experiments with two specimens of C-SiC composite, one at room temperature and the other at 1750 °C are shown in Figs. 12 and 13. The tomography images in these cases were collected at a lower magnification/resolution (1.3 μm/pixel) that gave a field of view of 3.3 mm, sufficient to accommodate the larger width of these test specimens. With the lower resolution, and with the minimal density difference between the carbon fibers and the pyrolytic-carbon coatings, individual fibers were not visible in either the transverse or the axial sections of Figs. 12 and 13; also details of individual fibers breaking and sliding are not resolved. Nevertheless, the carbon fiber tows are clearly distinguished from the denser SiC matrix. Our main focus in these experiments was to investigate the damage within and outside the tows in the matrix and study the interactions of damage with features in the structure of the woven composite. The image quality was identical in images collected at room temperature and high temperature.

Cracks were observed in the matrix approximately normal to the loading direction after applying a relatively small load (<20% of the failure load) at both temperatures. These first cracks (outlined by yellow boxes in the axial slices in Figs. 12 and 13) formed at locations where there was a relatively thin layer of matrix between the surface of the composite and an underlying transverse fiber tow. With increasing load, the cracks grew through the transverse tows and deflected when they met an underlying longitudinal tow. At low temperature the deflection involved formation of multiple splitting cracks within the longitudinal tow (e.g., Fig. 12(c)), whereas at high temperature the deflection involved a single crack growing along the edge of the longitudinal fiber tow (e.g., Fig. 13(c)). Further experiments are needed to determine whether similar differences in crack paths occur with loading in other directions relative to the fiber architecture.

IV. CONCLUSIONS

The acquisition of high-resolution 3D images under load at very high temperatures offers an opportunity to transform the way in which material development and qualification are

carried out.[10] The images reveal details about the evolution of damage mechanisms that would otherwise remain invisible. One key future use of this test system is in the development of virtual tests. The qualitative observations of damage emerging from the 3D *in situ* imaging tell us what mechanisms must be represented in a high-fidelity simulation, while quantitative measurements of, e.g., the displacement vectors of internal cracks serve to calibrate the nonlinear fracture cohesive laws that govern crack evolution in the simulations.

The utility of the instrument is evident in the examples of observations of damage development in two different fiber-reinforced ceramic composite materials at room temperature and at 1750 °C. The *in situ* tomography images allow the evolution of subcritical cracking in the fibers and matrices in the interior of the composites to be followed as an applied tensile load is increased. The trade-off in image quality, resolution, and scan speed with use of monochromatic or white-light radiation, the use of different image processing algorithms and the use of different magnifications was discussed.

Nevertheless, the challenge of conducting experiments at very high temperature is extreme, partly because of the difficulty of placing instrumentation near the test specimen without perturbing image quality. We have demonstrated a robust pyrometer system that meets the requirement of not being sited on the specimen and measures the temperature of the specimen continuously to within 20 °C while running tomography scans. Measurements using a calibration test specimen with an embedded thermocouple verify the pyrometry measurements. These measurements confirm that the instrument is capable of operating with specimen temperatures above 2000 °C in flowing gas environments (either inert or active).

Several system improvements remain to be accomplished. A method of reducing the uncertainty in the temperature on the surface of the specimen to approximately 1 °C would be very valuable. The development of digital image correlation methods, similar to those used effectively in CT for polymer matrix composites, but applicable to ceramic matrix materials, would improve the accuracy of crack displacement measurements by an order of magnitude, and correspondingly improve the accuracy of the calibration of fracture laws. Finally, algorithms that can quantify damage automatically by the analysis of 3D images would overcome a severe bottleneck. Because available image analysis tools were developed primarily for medical applications, they do not automatically identify damage of interest in materials engineering, such as cracking and crack displacements; such analysis of the data from a single test typically consumes several weeks when carried out by augmenting available automatic image analysis with human decisions.

ACKNOWLEDGMENTS

This work was supported by the U.S. Air Force Office of Scientific Research (AFOSR) (Dr. Ali Sayir) and National Aeronautics and Space Administration (NASA) (Dr. Anthony Calomino) under the National Hypersonics Science Center for Materials and Structures (AFOSR Prime Contract No. FA9550-09-1-0477 to Teledyne Scientific with sub-contract to the University of California, Berkeley). We are grateful for use of the x-ray micro-tomography beamline (8.3.2) at the Advanced Light Source, which is supported by the Director, Office of Science, Office of Basic Energy Sciences, of the U.S. Department of Energy under Contract No. DE-AC02-05CH11231.

[1] J. C. Zhao and J. H. Westbrook, MRS Bull. **28**(9), 622 (2003).
[2] S. Schmidt, S. Beyer, H. Immich, H. Knabe, R. Meistring, and A. Gessler, Int. J. Appl. Ceram. Technol. **2**(2), 85 (2005).
[3] D. B. Marshall and B. N. Cox, Annu. Rev. Mater. Res. **38**, 425 (2008).
[4] G. N. Morscher, H. M. Yun, and J. A. DiCarlo, J. Am. Ceram. Soc. **88**(1), 146 (2005).
[5] K. Nakano, A. Kamiya, Y. Nishino, T. Imura, and T. W. Chou, J. Am. Ceram. Soc. **78**(10), 2811 (1995).
[6] J. Aveston, G. A. Cooper, and A. Kelly, "Properties of fiber composites," in *Conference Proceedings of the National Physical Laboratory, Surrey, England*, 1971.
[7] D. B. Marshall and A. G. Evans, J. Am. Ceram. Soc. **68**(5), 225 (1985).
[8] D. B. Marshall and W. C. Oliver, J. Am. Ceram. Soc. **70**(8), 542 (1987).
[9] F. Rebillat, J. Lamon, R. Naslain, E. Lara-Curzio, M. K. Ferber, and M. Theodore, J. Am. Ceram. Soc. **81**(9), 2315 (1998).
[10] B. N. Cox, H. A. Bale, M. Begley, M. Blacklock, B.-C. Do, T. Fast, M. Naderi, M. Novak, V. P. Rajan, R. G. Rinaldi, R. O. Ritchie, M. N. Rossol, J. H. Shaw, O. Sudre, Q. D. Yang, F. W. Zok, and D. B. Marshall, Annu. Rev. Mater. Res. **44**(1), 479–529 (2014).
[11] B. Cox and Q. D. Yang, Science **314**(5802), 1102 (2006).
[12] Q. D. Yang, B. N. Cox, X. J. Fang, and Z. Q. Zhou, J. Eng. Mater.-Trans. ASME **133**(1), 11002 (2011).
[13] J. Allison, P. Collins, and G. Spanos, in *1st World Congress on Integrated Computational Materials Engineering (ICME), TMS, Seven Springs Mountain Resort, Seven Springs, PA*, 2011.
[14] T. M. Pollock, J. E. Allison, D. G. Backman, M. C. Boyce, M. Gersh, E. A. Holm, R. LeSar, M. Long, A. C. Powell, Jr., J. J. Schirra, D. D. Whitis, and C. Woodward, *Integrated Computational Materials Engineering: A Transformational Discipline for Improved Competitiveness and National Security* (National Research Council, Washington, D.C., 2008).
[15] H. A. Bale, A. Haboub, A. A. MacDowell, J. R. Nasiatka, D. Y. Parkinson, B. N. Cox, D. B. Marshall, and R. O. Ritchie, Nat. Mater. **12**(1), 40 (2013).
[16] S. R. Stock, Int. Mater. Rev. **53**(3), 129 (2008).
[17] H. Bale, M. Blacklock, M. R. Begley, D. B. Marshall, B. N. Cox, and R. O. Ritchie, J. Am. Ceram. Soc. **95**(1), 392 (2012).
[18] C. Chateau, L. Gelebart, M. Bornert, J. Crepin, E. Boller, C. Sauder, and W. Ludwig, Compos. Sci. Technol. **71**(6), 916 (2011).
[19] A. Sakdinawat and D. Attwood, Nat. Photon. **4**(12), 840 (2010).
[20] D. Bellet, B. Gorges, A. Dallery, P. Bernard, E. Pereiro, and J. Baruchel, J. Appl. Crystallogr. **36**, 366 (2003).
[21] Y. B. Wang, T. Uchida, F. Westferro, M. L. Rivers, N. Nishiyama, J. Gebhardt, C. E. Lesher, and S. R. Sutton, Rev. Sci. Instrum. **76**(7), 073709 (2005).
[22] P. Wright, X. Fu, I. Sinclair, and S. M. Spearing, J. Compos. Mater. **42**(19), 1993 (2008).
[23] A. J. Moffat, P. Wright, J. Y. Buffiere, I. Sinclair, and S. M. Spearing, Scr. Mater. **59**(10), 1043 (2008).
[24] T. Fast, A. E. Scott, H. A. Bale, and B. N. Cox, "Topological and Euclidean Metrics for Stochastic Fiber Bundles," J. Mech. Phys. Sol., 2014 (submitted).
[25] A. A. MacDowell, D. Y. Parkinson, A. Haboub, E. Schaible, J. R. Nasiatka, C. A. Yee, J. R. Jameson, J. B. Ajo-Franklin, C. R. Brodersen, and A. J. McElrone, Proc. SPIE **8506**, 850618 (2012).
[26] R. Grupp, F. Henkel, M. Nothe, J. Banhart, B. Kieback, and A. Haibel, J. Synchrotron Radiat. **16**, 524 (2009).
[27] P. Sarin, W. Yoon, K. Jurkschat, P. Zschack, and W. M. Kriven, Rev. Sci. Instrum. **77**(9), 093906 (2006).
[28] M. Dierick, B. Masschaele, and L. Van Hoorebeke, Meas. Sci. Technol. **15**(7), 1366 (2004).
[29] C. A. Schneider, W. S. Rasband, and K. W. Eliceiri, Nat. Methods **9**(7), 671 (2012).
[30] A. Groso, R. Abela, and M. Stampanoni, Opt. Express. **14**(18), 8103 (2006).
[31] Y. De Witte, M. Boone, J. Vlassenbroeck, M. Dierick, and L. Van Hoorebeke, J. Opt. Soc. Am. A **26**(4), 890 (2009).